Panel Method

For the panel method, the panel composed academic and faculty experts in the field of sustainability from various Canadian universities including Ryerson University, University of Western Ontario, University of Toronto, and University of Ontario Institute of Technology.

From: Energy Sustainability, 2020

Related terms:
Boundary Layer, Airfoils, Propellers, Angle-of-Attack, Computational Fluid Dynamic, Reynolds-Averaged Navier-Stokes

Propellers

Volker Bertram, in Practical Ship Hydrodynamics (Second Edition), 2012

2.3.5 Boundary Element Methods

Panel methods were developed to overcome the disadvantage of an incomplete geometry model. Panel methods also model the blade thickness and include the hub in the numerical model. The development of panel methods for propellers was apparently not an easy task. After the ship hull flow could be treated by panel methods it took another decade until the late 1980s before the first successful panel approaches were established for propellers. The implementation of a robust Kutta condition is a decisive element of each propeller panel code, since it controls torque and thrust. In principle, there exist many possibilities to create panel codes, depending on panel type and the formulation of the problem (e.g. Kerwin et al. 1987). The following panel types are found:

- dipole panels;
- source panels;
- mix of dipole panels and source panels.

The problem may be formulated as:

- direct formulation (potential formulation); potential itself is the unknown;
- indirect formulation (velocity formulation); source or dipole strength is unknown.

For indirect formulations, Kerwin et al. (1987) show how a dipole-based formulation can be transformed to an equivalent vortex-based formulation.

The majority of the panel codes used for propellers follows Morino's approach (Morino and Kuo 1974, Morino 1975). Morino's approach is a direct formulation, i.e. it solves directly for the potential and determines velocities by numerical differentiation. The approach uses exclusively dipole panels, which discretize the surfaces of the propeller blades, the hub, and part of the wakes of each blade. The Kutta condition demands that at the trailing edge the pressure difference between face and back should vanish. This couples the dipoles on the wake to the dipoles on the propeller. The panels in the wake all have the same strength for steady flow conditions. The pitch of the wake is either specified by largely empirical relations or determined iteratively as part of the solution. The Kutta condition enforcing a vanishing pressure jump at the trailing edge is a non-linear condition requiring an iterative solution. The numerical implementation of the Kutta condition requires great care, since simplifications or conceptual errors in the physical model may strongly affect the computed lift forces.

The main problems of these methods lie in:

- numerical realization of the Kutta condition (stagnation point at the trailing edge);
- numerical (accurate) determination of velocity and pressure fields.

In the 1990s, panel methods were presented that were also capable of solving the problem for time-dependent inflow and ducted propellers (e.g. Kinnas 1996).

Systems Analysis & Life Cycle Analysis

Thomas P. Gloria, in Encyclopedia of Sustainable Technologies, 2017

How Weighting Factors Are Determined

Methods to derive weighting factors can be classified in four different categories, namely:

Panel methods, where a group of experts representing different stakeholders are asked to provide their weighting factors. Panels can be composed of nonexpert stakeholders (Huppes and van Oers, 2011), experts from various backgrounds (academia, industry, politicians) (Saling et al., 2002; Goedkoop and Spriensma, 2001), or using a multiattribute decision-making approach using methods such as simple additive weighting and the analytical hierarchy process (Gloria et al., 2007; Benoit and Rousseaux, 2003; Koffler et al., 2008; Pizzol et al., 2016; Huppes and van Oers, 2011).

Monetization methods, where the weighting factors are determined by monetary costs according to the estimated economic damage incurred in an impact category or the cost to prevent the damage itself (Pizzol et al., 2016; Huppes and van Oers, 2011). Monetary methods can be based on observed preferences, such as the marginal value of a quality adjusted life year as the basis of the potential economic production per capita per year (Steen, 1999a,b); revealed preferences based on hedonic pricing of the marginal value of indirectly affected goods (Finnveden et al., 2006); and Stated preferences, based on the marginal value of products determined by contingent valuation (Itsubo et al., 2015; 2012; Pizzol et al., 2016).

Distance-to-target methods, where the weighting factors are calculated as a function of some type of target values, which are often based on regulatory normative targets (e.g., greenhouse gas emissions targets, smog emission restrictions) or political decisions (Castellani et al., 2016; Pizzol et al., 2016; Huppes and van Oers, 2011).

Binary weighting methods, where impacts are assigned either no weight or equal importance, based on criteria selected by the practitioner or stakeholder group. Equal weighting can be interpreted as neutral weighting, but it is not (Pizzol et al., 2016). Equal weighting can be found in unpublished methods such as the Higg Index employed by the Sustainable Apparel Coalition (2016). Single impact category investigations such as carbon footprinting, water footprint assessment, do not explicitly state that they include binary weighting, whereby implicitly all other categories are weighted zero (Pizzol et al., 2016).

Weighting methods can also be categorized as value based or preference based. Value-based methods such as Powell et al. (1997) and Myllyviita et al. (2014) are the

condition where one value is identified as being more important than another and must be met before others can be considered (e.g., no genetically modified crops). Preference-based methods, such as Soares et al. (2006), and Heijungs (2008), are determined by the preferences set up by an individual or stakeholder group. Preference-based methods are more generally applied in LCA due to the limitations of the value-based approach to support decision-making with more than two values (Huppes and van Oers, 2011).

In their simplest form, impact category weights are unitless figures, representing percent of preference, as shown in **Fig. 1**, is set of weights developed by the panel method utilizing the analytical hierarchy approach for the US EPA TRACI methodology set of impacts used in the building for environmental and economic sustainability methodology (Gloria et al., 2007).

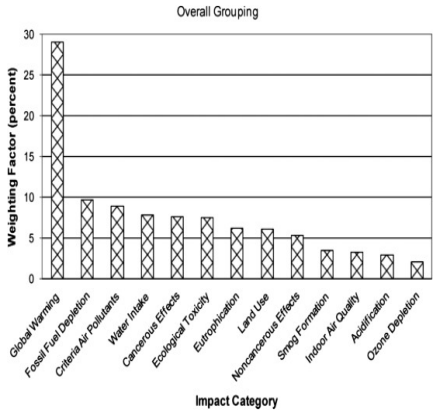

Fig. 1. Example of a set of weights to assist in preferable purchasing decision support.

The weights can be further delineated by stakeholder group as shown in **Fig. 2**. Seager and Linkov (2008) observe high uncertainty of results that can be realized by the variability over stakeholder groups.

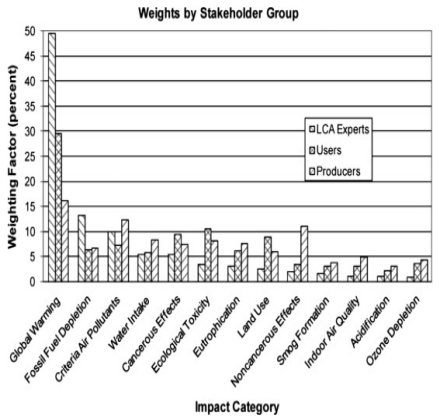

Fig. 2. Example of a set of weights by stakeholder group to assist in preferable purchasing decision support.

Read full chapter

URL: https://www.sciencedirect.com/science/article/pii/B9780124095489100703

Wind Energy

M. Karimirad, in Comprehensive Renewable Energy, 2012

2.09.4.2 Hydrodynamic Loads

Hydrodynamic loads on the floater consist of nonlinear and linear viscous drag effects, currents, radiation (linear potential drag) and diffraction (wave scattering), buoyancy (restoring forces), integration of the dynamic pressure over the wetted surface (Froude–Krylov), and inertia forces. A combination of the pressure integration method, the boundary element method, and the Morison formula can be used to represent the hydrodynamic loading. The linear wave theory may be used in deepwater areas, while in shallow water the linear wave theory is not accurate as the waves are generally nonlinear. It was shown that [15] for offshore wind turbines, nonlinear (second-order), irregular waves can better describe waves in shallow waters. Considering the instantaneous position of the structure in finding the loads add some nonlinearity. These hydrodynamic nonlinearities are mainly active in the resonant responses, which influence the power production and structural responses at low natural frequencies.

Considering the size and type of the support structure and turbine, wave loading may be significant and can be the main cause of fatigue and extreme loads that should be investigated in coupled analysis. Hence, the selection of a suitable method of determining the hydrodynamic loads can have an important effect on the cost of the system and its ability to withstand environmental and operational loads.

The panel method, Morison formula, pressure integration method, or combination of these methods can be used to calculate the hydrodynamic forces. The selection of the method should be concept-dependent. Some of the hydrodynamic aspects for an FWT that may be considered depending on the concept and site specification are listed below [16, 17]:

- Appropriate wave kinematics models
- Hydrodynamic models considering the water depth, sea climates, and support structures
- Extreme hydrodynamic loading, including breaking waves, using nonlinear wave theories and appropriate corrections
- Stochastic hydrodynamic loading using linear wave theories with empirical corrections
- Consideration of both slender and large-volume structures depending on the support structure of the FWT.

The Morison formula is practical for slender structures where the dimension of the structure is small compared to the wavelength, that is, $D_{ch} < 0.2\lambda$ [16], where D_{ch} is the characteristic diameter and λ is the wavelength. In other words, it is assumed that the structure does not have significant effect on the waves. The hydrodynamic

forces through the Morison formula include the inertial and quadratic viscous excitation forces. The inertial forces in the Morison formula consist of diffraction and Froude–Krylov forces for a fixed structure. For a floating structure, the added mass forces are included in the Morison formula through relative acceleration as well and the damping forces appear through the relative velocity.

Equation [8] shows the hydrodynamic forces per unit length on the floater based on the Morison formula, which was extended to account for the instantaneous position of the structure for FWTs [16].

$$d\boldsymbol{F} = \frac{\rho_w}{2} C_d D_{cyl} |u_r| u_r + \rho_w \frac{\pi D_{cyl}^2}{4} C_m \dot{u}_r + \rho_w \frac{\pi D_{cyl}^2}{4} C_m \dot{u}_W \quad [8]$$

$$u_r = u_W - u_B \quad [9]$$

where ρ_w is the mass density of seawater, D_{cyl} is the cylinder diameter, $\dot{u}_r$ and u_r are the horizontal relative acceleration and velocity between the water particle velocity u_W and the velocity of the body u_B (eqn [9]), respectively, and C_m and C_d are the added mass and quadratic drag coefficients, respectively.

The first term is the quadratic viscous drag force, the second term includes the diffraction and added mass forces, and the third term is the Froude–Krylov force (FK term). A linear drag term $C_1 u_r$ can be added to the Morison formula as well, where C_1 is the linear drag coefficient. The positive force direction is in the wave propagation direction. C_d and C_1 have to be empirically determined and are dependent on many parameters as the Reynolds number, Keulegan–Carpenter (KC) number, a relative current number, and surface roughness ratio [16].

For large-volume structures, the diffraction becomes important. The MacCamy–Fuchs correction for the inertia coefficient in some cases can be applied. Based on the panel method (BEM), the added mass coefficient for a circular cylinder is equal to 1, which corresponds to the diffraction part of the Morison formula. The Froude–Krylov contribution can be found by pressure integration over the circumference; for a cylinder in a horizontal direction, the added mass coefficient is equal to 1. Therefore, the inertia coefficient for a slender circular member is 2. It is possible to use the pressure integration method to calculate the Froude–Krylov part of the Morison formula and just apply the diffraction part through the Morison formula.

For an FWT, the instantaneous position should be accounted for when updating the hydrodynamic forces. Hence, the original Morison formulation should be changed using the relative acceleration and velocities. The relative velocity will be applied to the quadratic viscous part. The pressure integration method and the Morison formula use the updated wave acceleration at the instantaneous position. The geometrical updating adds some nonlinear hydrodynamic loading that can excite the low natural frequencies of the spar.

Based on second-order wave theory, the mean drift, slowly varying (difference frequency) and sum frequency forces, drift-added mass, and damping can be added to the above linear wave theory. The Morison formula combined with the pressure integration method is a practical approach to model the hydrodynamic forces for a spar-type wind turbine. Using the modified linear wave theory accounting for the wave kinematics up to the wave elevation and the pressure integration method in transversal directions (Froude–Krylov), the mean drift forces were considered in this chapter. Moreover, the sum frequency forces were considered by using the instantaneous position of the structure to calculate the hydrodynamic forces.

Theoretical and numerical methods

Anthony F Molland, Stephen R Turnock, in Marine Rudders and Control Surfaces, 2007

6.2.3 Coupled boundary layer

The surface panel method can be enhanced to include the effect of viscosity through coupling a method for evaluating a solution of the thin boundary layer approximations to the full N–S equations along a series of surface streamlines. There are two approaches:

(1) The geometry of the body in question is altered by increasing its size in the surface normal direction by an amount equal to the displacement thickness of the local boundary layer, Section 3.2.13 and Figure 3.13.

(2) Rather than the imposed zero normal relative velocity condition on the body surface, a flux of momentum is applied. The magnitude of this flux (transpiration velocity V_t) is proportional to the rate of momentum exchange at the edge of the boundary layer and is given by

$$V_t = \frac{\partial}{\partial s}(V_\delta \delta^*) \quad (6.37)$$

where s is the streamwise direction, V_δ the velocity at the edge of the boundary layer and δ^* the local displacement thickness along a streamline.

The three steps necessary to include the boundary layer growth in the flow solution are:

1. solve the potential flow over the body and obtain the surface pressure distribution;
2. using the pressure distribution, calculate boundary-layer characteristics and
3. modify the surface boundary conditions for the potential flow, and solve for the next iteration.

Considerable effort has been expended in developing accurate methods for solving the thin boundary-layer equations. Particular attention has been given to the prediction of laminar-turbulent transition, attached small separation bubbles and the capture of large zones of separation. In many cases, these methods and their associated mathematical complexity and significant computational effort, are in the process of being superseded by the complete N–S solvers described in Equation (6.3).

Theoretical methods that have the limited objective of predicting overall characteristics of the boundary layer, for example, momentum thickness, displacement thickness and skin friction, rather than details of the actual flow, are more straightforward to apply. For the purpose of improving rudder performance prediction, such methods are all that are needed to modify the potential flow.

The modification is split into a number of components (see Figure 6.3): prediction of the laminar boundary-layer growth from either a sharp edge or stagnation point, estimate of when transition to turbulence occurs, turbulent boundary layer growth and an estimation of whether the flow will separate

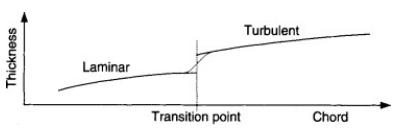

Figure 6.3. Schematic for smoothing the transition point discontinuity

$$\frac{1}{2} C_f = \frac{\theta}{V_\delta} \cdot \frac{dV_\delta}{ds}(H+2) + \frac{d\theta}{ds} \quad (6.38)$$

where the shape factor $H = \delta^*/\theta$, θ is the boundary layer momentum thickness and δ^* the boundary layer displacement thickness.

6.2.3.1 Prediction of separation

Estimates of the likely point of flow separation on the body surface can be made using either the shape factor H or the skin friction coefficient C_f as the criterion for separation. For example, the C_f law given by Ludwieg and Tillmann [6.18];

$$C_f = 0.246 \times 10^{-0.678H} R_\theta^{-0.268} \tag{6.39}$$

which predicts $C_f = 0$ as H tends to infinity. An exact value of H corresponding to separation cannot be specified, but a range between 1.8 and 2.4 has been quoted [6.19]. For a NACA 0020 [6.20] section foil at 20° angle of attack, predictions of the chordwise point of separation, using this range of H values, are given in Table 6.1.

Table 6.1. Predicted flow separation on NACA0020 at 20° angle of attack

H	1.8	1.9	2.0	2.1	2.2	2.3	2.4
% Chord	57.3	64.8	72.1	76.6	79.5	82.5	82.5

The predicted position varied substantially, between 57% and 83% chord, for the range of H values. Without knowing the precise point of flow separation, the more reliable means is to use the C_f values. In this case, $C_f \to 0$ occurred at 81.7%c, which lies within the quoted range of H.

The starting point for applying such 2-D calculations is the definition of a suitable streamline across the 3-D rudder surface. Methods of varying levels of complexity can be applied to trace the streamline forward to a stagnation point or sharp leading edge, and backward to a point of separation or a trailing edge. Once such a streamline has been found the coordinates of the underlying surface should be used to define a parametric curve with known values of tangential velocity at specified points along its length. The integral boundary layer method can then be applied with an appropriate level of discretisation, which is likely to be different from that used for the surface panels. In some methods, 3-D effects due to streamline curvature normal to the flow direction are used to modify the integral boundary-layer equation. For most rudder-like flows these effects are small except near the tip.

Although small laminar separations can be handled, only the initiation of large zones of separation can be predicted. Such information can provide valuable insight into the limitations of a particular surface panel calculation. If necessary, the edge of the zone of separation can be panelled and the modified potential flow represented.

Thin Airfoil Theory

E.L. Houghton, ... Daniel T. Valentine, in Aerodynamics for Engineering Students (Seventh Edition), 2017

6.10 Computational (Panel) Methods for Two-Dimensional Lifting Flows

We now describe the extension of the computational method described in Section 5.5 to two-dimensional lifting flows. The basic panel method was developed by a group led by Hess and Smith [28] at Douglas Aircraft in the late 1950s and early 1960s. Their method applied surface distributions of sources and doublets (the latter required to solve the lifting problem). A panel method that applies vortex panels appears to have been first developed by Rubbert [29] at Boeing to solve lifting flows. Its two-dimensional version can be applied to airfoil sections of any thickness and camber. In essence, to generate the circulation necessary for the production of lift, vorticity in some form must be introduced into the modeling of the flow.

In the panel method for nonlifting bodies, as described in Section 5.5, a surface distribution of sources is applied. For the lifting case, the airfoil section can be modeled by vortex panels in the form of straight-line segments with the strength, which can be distributed over panels that model the airfoil contour itself, as shown in Fig. 6.22. This procedure allows us to model the airfoil shape completely (thickness and camber) using vortex panels only. This is the approach we use in this section to examine two-dimensional airfoils.

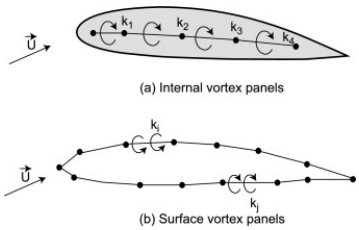

Figure 6.22. Vortex panels: (a) internal; (b) surface.

The central problem of extending the panel method to lifting flows is satisfying the Kutta condition (see Section 6.1.1). It is not possible with a computational scheme to do this directly; instead, the aim is to satisfy some of the implied conditions:

1. The streamline leaves the trailing edge with a direction along the bisector of the trailing-edge angle.
2. As the trailing edge is approached, the velocity magnitudes on the upper and lower surfaces approach the same limiting value.
3. In the practical case of an airfoil with a finite trailing-edge angle, the trailing edge must be a stagnation point; the common limiting value of (b), then, must be zero.
4. The source strength per unit length must be zero at the trailing edge.

Computational schemes use either conditions (a) or (b). It is not generally possible to satisfy (c) and (d) as well because, as will be shown, an overspecification of the problem results. The methods for satisfying (a) and (b) are illustrated in Fig. 6.23. For condition (a), an additional panel must be introduced oriented along the bisector of the trailing-edge angle. The value of the circulation is then fixed by requiring the normal velocity to be zero at the collocation point of the additional ($N+1$) panel. For condition (b), the magnitudes of the tangential velocity vectors at the collocation points of the two panels, which define the trailing edge, are required to be equal. Hess [30] showed that condition (b) gives more accurate results than condition (a), other things being equal. The use of surface, rather than interior, vorticity panels is also preferable for computational accuracy.

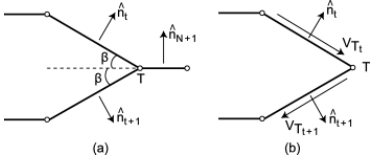

Figure 6.23. Two methods of implementing the Kutta condition at the trailing edge *T*.

To use vortex panels alone, each of the *N* panels carries a vortex distribution of uniform strength per unit length, γ_i ($i = 1, 2, \ldots, N$). In general, the vortex strength varies from panel to panel. Let $i = t$ for the panel on the upper surface at the trailing edge so that $i = t + 1$ for the panel on the lower surface at the trailing edge. Condition (b) is equivalent to requiring that

$$\gamma_t = -\gamma_{t+1} \tag{6.98}$$

The normal velocity component at the collocation point of each panel must be zero, as it is for the nonlifting case. This gives *N* conditions to be satisfied for each of the *N* panels. Thus, when we take into account condition Eq. (6.98), there are $N + 1$ conditions to be satisfied in total. Unfortunately, there are only *N* unknown vortex strengths, so it is not possible to satisfy all $N + 1$ conditions. Thus, in order to proceed further, it is necessary to ignore the requirement that the normal velocity be zero for one panel. This is unsatisfactory since it is not at all clear which panel is the best choice.

An alternative and more satisfactory method is to distribute both sources and vortices of uniform strength per unit length over each panel. In this case, though, the vortex strength is the same for all panels:

$$\gamma_i = \gamma (i = 1, 2, \ldots, N) \tag{6.99}$$

Thus there are now $N + 1$ unknown quantities—namely, the *N* source strengths and the uniform vortex strength per unit length γ to match the $N + 1$ conditions. With this approach it is perfectly feasible to use internal vortex instead of surface panels. However, the internal panels must carry vortices that are either of uniform strength or of predetermined variable strength, providing that the variation is characterized by a single unknown parameter. Generally, however, surface vortex panels lead to better results. Also condition (a) can be used in place of condition (b). Again, however, condition (b) generally gives more accurate results.

A practical panel method for lifting flows around airfoils is described in some detail next. It uses condition (b) and is based on a combination of surface vortex panels, of uniform strength, and source panels. First, however, it is necessary to show how the normal and tangential influence coefficients for vortex panels may be evaluated. It turns out that the procedure is very similar to that for source panels.

The velocity at point *P* due to vortices on an element of length $\delta\xi$ in Fig. 6.24 is given by

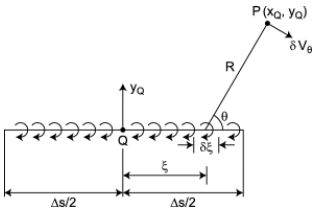

Figure 6.24. Thin airfoil modeled as a vortex sheet.

$$\delta V_\theta = \frac{\gamma}{R} d\xi \tag{6.100}$$

where $\gamma d\xi$ replaces $\Gamma/(2\pi)$ used in Section 5.3.2. δV_θ is oriented at angle θ as shown. Therefore, the velocity components in the panel-based coordinate directions (i.e., in the x_Q and y_Q directions) are given by

$$\delta V_{x_Q} = \delta V_\theta \sin\theta = \frac{\gamma y_Q}{(x_Q - \xi)^2 + y_Q^2} \delta\xi \tag{6.101}$$

$$\delta V_{y_Q} = -\delta V_\theta \cos\theta = -\frac{\gamma (x_Q - \xi)}{(x_Q - \xi)^2 + y_Q^2} \delta\xi \tag{6.102}$$

To obtain the corresponding velocity components at *P* due to all vortices on the panel, we integrate along the length of the panel to get

$$\begin{aligned} V_{x_Q} &= \gamma \int_{-\Delta s/2}^{\Delta s/2} \frac{y_Q}{(x_Q - \xi)^2 + y_Q^2} d\xi \\ &= \gamma \left[\tan^{-1}\left(\frac{x_Q + \Delta s/2}{y_Q} \right) - \tan^{-1}\left(\frac{x_Q - \Delta s/2}{y_Q} \right) \right] \end{aligned} \tag{6.103}$$

$$V_{y_Q} = -\gamma \int_{-\Delta s/2}^{\Delta s/2} \frac{x_Q - \xi}{(x_Q - \xi)^2 + y_Q^2} d\xi = -\frac{\gamma}{2} \ln \left[\frac{(x_Q + \Delta s/2)^2 + y_Q^2}{(x_Q - \Delta s/2)^2 + y_Q^2} \right] \tag{6.104}$$

Following the basic method described in Section 5.5, we introduce normal and tangential influence coefficients, N'_{ij} and T'_{ij}; the primes distinguish these coefficients from those introduced in Section 5.5 for the source panels. N'_{ij} and T'_{ij} represent the normal and tangential velocity components at collocation point *i* due to vortices of unit strength per unit length distributed on panel *j*.

Let $\hat{t}_i$ and $\hat{n}_i (i = 1, 2, \ldots, N)$ denote the unit tangent and normal vectors for each panel, and let point *P* correspond to collocation point *i*. Then in vector form we get the velocity at collocation point *i*:

$$\vec{V}_{PQ} = V_{x_Q} \hat{t}_j + V_{y_Q} \hat{n}_j$$

To obtain the components of this velocity vector perpendicular and tangential to panel *i*, we take the scalar product of the velocity vector with $\hat{n}_i$ and $\hat{t}_i$, respectively. If furthermore γ is set equal to 1 in Eqs. (6.103) and (6.104), we obtain the following expressions for the influence coefficients:

$$\begin{aligned} N'_{ij} &= \vec{V}_{PQ} \cdot \hat{n}_i = V_{x_Q} \hat{n}_i \cdot \hat{t}_j + V_{y_Q} \hat{n}_i \cdot \hat{n}_j; \\ T'_{ij} &= \vec{V}_{PQ} \cdot \hat{t}_i = V_{x_Q} \hat{t}_i \cdot \hat{t}_j + V_{y_Q} \hat{t}_i \cdot \hat{n}_j \end{aligned} \tag{6.105}$$

Comparing Eqs. (6.103) and (6.105) for the vortices and the corresponding expressions for the source panels shows that

$$[V_{x_q}]_{\text{vortices}} = [V_{y_q}]_{\text{sources}} \quad \text{and} \quad [V_{y_q}]_{\text{vortices}} = -[V_{x_q}]_{\text{sources}} \tag{6.106}$$

With these results, it is now possible to describe how the basic panel method of Section 5.5 may be extended to lifting airfoils.

Each of the *N* panels now carries a source distribution of strength σ_i per unit length and a vortex distribution of strength γ per unit length. Thus there are now $N + 1$ unknown quantities, so the $N \times N$ influence coefficient matrices N_{ij} and T_{ij} corresponding to the sources must be expanded to $N \times (N + 1)$. The $(N + 1)$ column at this point contains the velocities induced at the collocation points by

vortices of unit strength per unit length on all of the panels. Thus $N_{i,\,N+1}$ represents the normal velocity at the ith collocation point induced by the vortices over all panels and similarly for $T_{i,\,N+1}$. Thus, using Eq. (6.105),

$$N_{i,\,N+1} = \sum_{j=1}^{N} N'_{i,\,j}, \quad \text{and} \quad T_{i,N+1} = \sum_{j=1}^{N} T'_{i,\,j} \tag{6.107}$$

In a similar fashion as for the nonlifting case described in Section 5.5, the total normal velocity at each collocation point—due to the net effect of all sources, vortices, and the oncoming flow—must be zero. This can be written in the form

$$\sum_{j=1}^{N} \sigma_j N_{ij} + \gamma N_{i,\,N+1} + \vec{U} \cdot \hat{n}_i = 0, \quad (i = 1, 2, \ldots, N) \tag{6.108}$$

where the first term represents the sources, the second term represents the vortices, and the third term is the onset (or oncoming) flow. These N equations are supplemented by imposing condition (b). The simplest way to do this is to equate the magnitudes of the tangential velocities at the collocation point of the two panels defining the trailing edge (see Fig. 6.23(b)). Remember that the unit tangent vectors $\hat{t}_t$ and $\hat{t}_{t+1}$ are in opposite directions, so condition (b) can be expressed mathematically as

$$\sum_{j=1}^{N} \sigma_j T_{t,\,j} + \gamma T_{t,\,N+1} + \vec{U} \cdot \hat{t}_t = -\left(\sum_{j=1}^{N} \sigma_j T_{t+1,\,j} + \gamma T_{t+1,\,N+1} + \vec{U} \cdot \hat{t}_{t+1} \right) \tag{6.109}$$

Equations (6.108) and (6.109) combine to form a matrix equation written as

$$\mathbf{M}\mathbf{a} = \mathbf{b} \tag{6.110}$$

where **M** is an $(N+1) \times (N+1)$ matrix and **a** and **b** are $(N+1)$ column vectors. The elements of the matrix and vectors are as follows:

$$\begin{aligned} M_{i,\,j} &= N_{i,\,j}, \quad i = 1, 2, \ldots, N, \quad j = 1, 2, \ldots, N+1 \\ M_{N+1,\,j} &= T_{t,\,j} + T_{t+1,\,j}, \quad j = 1, 2, \ldots, N+1 \\ a_i &= \sigma_i, \quad i = 1, 2, \ldots, N, \quad \text{and} \quad a_{N+1} = \gamma \\ b_i &= -\vec{U} \cdot \hat{n}_i, \quad i = 1, 2, \ldots, N, \quad \text{and} \quad b_{N+1} = -\vec{U} \cdot \left(\hat{t}_t + \hat{t}_{t+1} \right) \end{aligned}$$

Systems of linear equations such as Eq. (6.110) can be readily solved numerically for unknowns a_i using standard methods (see Section 5.5). Also, it is now possible to see condition (c), requiring that the tangential velocities on the upper and lower surfaces tend to zero at the trailing edge, cannot be satisfied in this sort of numerical scheme. Condition (c) could be imposed approximately by requiring, say, that the tangential velocities on panels t and $t+1$ both be zero. Referring to Eq. (6.109), this approximate condition can be expressed mathematically as

$$\sum_{j=1}^{N} \sigma_j T_{t,\,j} + \gamma T_{t,\,N+1} + \vec{U} \cdot \hat{t}_t = 0$$

and

$$\sum_{j=1}^{N} \sigma_j T_{t+1,\,j} + \gamma T_{t+1,\,N+1} + \vec{U} \cdot \hat{t}_{t+1} = 0$$

Equation (6.109) is replaced by these two equations so that M in Eq. (6.110) is now a $(N+2) \times (N+1)$ matrix. At this point, the problem is overdetermined (i.e., there is one more equation than the number of unknowns), and (6.110) can no longer be solved for the vector **a**—that is, for the source and vortex strengths.

Calculating the influence coefficients is at the heart of any panel method. In Section 5.5, a MATLAB function was given for computing the influence coefficients for the nonlifting case and was used to solve the problem of flow around a NACA 0024 symmetric airfoil. In this section, we provide a MATLAB function to compute the influence coefficients due to additional vortices required for a lifting flow. It is applied to solve the flow around a NACA 4412 airfoil to demonstrate that the numerics agree with experiments and with the theoretical results already described.

Two modifications to `function InfluSour` from Section 5.5 are required to extend it to the lifting case.

1. The following loop is added at the beginning of the function:

```
NP1 = N + 1
for I = 1,N
  AN(I,NP1) = 0;
  AT(I,NP1) = pi;
end
```

   The additional lines initialize the values of the influence coefficients, $N_{i,\,N+1}$ and $T_{i,\,N+1}$, preparing them for calculation later in the program. Note that the initial value of $T_{i,\,N+1}$ is set at π because, in Eq. (6.107),

$$T'_{N+1,\,N+1} = N_{i,\,j} = \pi$$

   that is, the tangential velocity induced on a panel by vortices of unit strength per unit length distributed over the same panel is, from Eq. (6.106), the same as the normal velocity induced by sources of unit strength per unit length. This takes the value π.

2. The two lines of instruction that calculate the additional influence coefficients according to Eq. (6.107) are inserted below the last two command lines in the function:

```
AN(I,J) = VX * NTIJ + VY * NNIJ; % existing line
AT(I,J) = VX * TTIJ + VY * TNIJ; % existing line
AN(I,NP1) = AN (I,NP1) + VY * NTIJ - VX * NNIJ; % added
 line
AT(I,NP1) = AT (I,NP1) + VY * TTIJ - VX * TNIJ; % added
 line
```

The modified function is given here:

```
function [AN,AT,XC,YC,NHAT,THAT] = InfluSourV(XP,YP,N,NT,N
TP1)
% Influence coefficients for source distribution over a
% symmetric body.
%
NP1 = N + 1;
for J = 1:N
    AN(J,NP1) = 0;
    AT(J,NP1) = pi;
if J==1
  XPL = XP(N);
  YPL = YP(N);
else
  XPL = XP(J-1);
  YPL = YP(J-1);
end
XC(J) = 0.5*(XP(J) + XPL);
YC(J) = 0.5*(YP(J) + YPL);
S(J) = sqrt( (XP(J) - XPL)^2 + (YP(J) - YPL)^2 );
THAT(J,1) = (XP(J) - XPL)/S(J);
THAT(J,2) = (YP(J) - YPL)/S(J);
```

```
NHAT(J,1) = - THAT(J,2);
NHAT(J,2) =   THAT(J,1);
end
%Calculation of the influence coefficients.
for I = 1:N
for  J = 1:N
if I==J
AN(I,J) = pi;
AT(I,J) = 0;
else
DX = XC(I) - XC(J);
DY = YC(I) - YC(J);
XQ = DX*THAT(J,1) + DY*THAT(J,2);
YQ = DX*NHAT(J,1) + DY*NHAT(J,2);
VX = -0.5*(  log( (XQ + S(J)/2 )^2 + YQ*YQ )...
    -log( (XQ - S(J)/2 )^2 + YQ*YQ )  );
VY = -
( atan2((XQ + S(J)/2 ),YQ) - atan2((XQ - S(J)/2),YQ ));
NTIJ = 0;
NNIJ = 0;
TTIJ = 0;
TNIJ = 0;
for K = 1:2
NTIJ = NHAT(I,K)*THAT(J,K) + NTIJ;
NNIJ = NHAT(I,K)*NHAT(J,K) + NNIJ;
TTIJ = THAT(I,K)*THAT(J,K) + TTIJ;
TNIJ = THAT(I,K)*NHAT(J,K) + TNIJ;
end
AN(I,J) = VX*NTIJ + VY*NNIJ;
AT(I,J) = VX*TTIJ + VY*TNIJ;
AN(I,NP1) = AN(I,NP1) + VY*NTIJ - VX*NNIJ;
AT(I,NP1) = AT(I,NP1) + VY*TTIJ - VX*TNIJ;
end
end
end
for n = 1:NP1
    AN(NP1,n) = -(AT(NT,n) + AT(NTP1,n));
    AT(NP1,n) = 0;
end
AT(NP1,NP1) = pi;
```

Like the original routine presented in Section 5.5, this modified routine is primarily intended for educational purposes. Nevertheless, as shown by the example computation for the NACA 4412 airfoil presented next, a computer program based on this function and MATLAB matrix-inversion methods gives accurate results for pressure distribution and hence for coefficients of lift and pitching moment. The predictions of pressure distribution were compared with other computations and experiments at the same lift coefficient since the effective angle of attack was not known in the experiment.

The essential parts of the script used to create Fig. 6.25 are as follows:

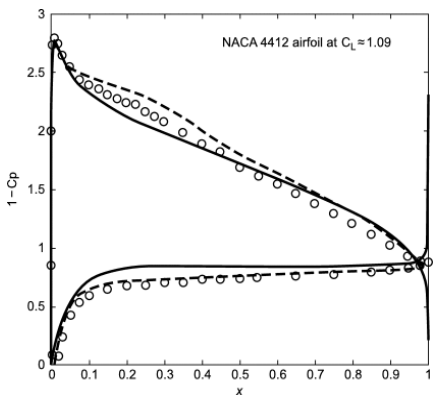

Figure 6.25. Solid line is the present prediction; dotted line is a prediction based on a code with viscous effects included; circles are experimental data.

```
 %
% NACA 4-digit airfoil: 4412
%
% clear;clc
c = 1;
Nthe = 201;
the = 0:-2*pi/Nthe:-pi;
x = (1 + cos(the) )/2;
m=4/100; p=4/10; t = 0.12;
yt = 5*t*c .* (.2969*x.^0.5 - .126*x ...
    - .3516*x.^2 + .2843*x.^3 - .1015*x.^4); %yt(length(x)
)=0;
for n=1:length(x)
  if x <= p
    yc(n) = (m*c/p)*(2*p*x(n)-x(n)^2);
  else
    yc(n) = (m*c/(1-p)^2)*((1-2*p) + 2*p*x(n) - x(n)^2);
  end
end
XPU = x; YPU = yt + yc;
for n = 1:length(x)-1
    XPL(n) = x(length(x)-n);
    YPL(n) = yc(length(x)-n) - yt(length(x)-n);
end
XP = [XPU(1:end) XPL(1:end-1)];
YP = [YPU(1:end) YPL(1:end-1)];
% Inherent camber angle of attack = atan(0.022)*180/pi = 1
.3
alpha = 4.2; alp = pi*alpha/180; N = length(XP);
NT = 1; NTp1 = N;
% for m = 1:N
%     YP(m) = YP(m) - sin(alpha*pi/180)*XP(m);
% end
figure(1);plot(XP,YP,'-o')
%
[AN,AT,XC,YC,NHAT,THAT] = InfluSourV(XP,YP,N,NTp1,NT);
% uinfty = 1;
```

```
for j=1:N
b(j,1) =  cos(alp)*NHAT(j,1) + sin(alp)*NHAT(j,2);
end
 b(N+1,1) = - ( THAT(NT,1) + THAT(NT+1,1));
Sources = AN\b;
THAT(N+1,1) = 0; THAT(N+1,2) = 0;
ut = AT*Sources - THAT(:,1);
cp = 1 - ut.^2;
figure(2);
plot(XC,1-cp(1:end-1),'k')
xlabel(' x '),ylabel('  1-Cp '),axis([0 1 0 3])
title(' NACA 4412 airfoil at C_L \approx 1.09')
```

The NACA 4412 wing section was chosen to illustrate the panel method. It is moderately thick with moderate camber. The variation in pressure coefficient around this wing section at an angle of attack of 8 degrees is presented in the figure. Experimental data are compared with the computed results for 200 panels. Agreement between the computed data and the experimental data is satisfactory. Note that the predictions of pressure distribution are for the same lift coefficient, as determined by integrating the measured pressure. Agreement between the data and the predictions is remarkably good for this airfoil.

Read full chapter

URL: https://www.sciencedirect.com/science/article/pii/B9780081001943000067

Differential Methods with Algebraic Turbulence Models

Tuncer Cebeci, in Analysis of Turbulent Flows with Computer Programs (Third Edition), 2013

8.9.1 Viscous Effects

The viscous effects can be introduced into the panel method by (1) replacing the zero normal-velocity condition, Eq. (8.9.11), by a nonzero normal-velocity condition $V_{iw}(x)$ and by (2) satisfying the Kutta condition, Eq. (8.9.17), not on the surface of the airfoil trailing edge but at some distance away from the surface.

Here it will be assumed that the nonzero normal-velocity distribution $V_{iw}(x)$ along the surface of the airfoil and in its wake is known, together with the distance from the surface, say displacement thickness δ^*, where the Kutta condition is to be satisfied. We now describe how these two new conditions can be incorporated into the panel method.

To include the nonzero normal-velocity condition into the solution procedure, we write Eq. (8.9.18) as

$$\sum_{j=1}^{N} A_{ij}^{n} q_j + \tau \sum_{j=1}^{N} B_{ij}^{n} q_j + V_\infty \sin(\alpha - \theta_i) = v_{iw}(x_{m_i}) \tag{8.9.27}$$

To satisfy the Kutta condition at the normal distance δ^* from the surface of the trailing edge, called the "off-body" Kutta condition, the total velocities at the N-th and first off-body control points are again required to be equal. Since the normal velocity component is not zero, we write the off-body Kutta condition at distance δ^* as

$$(V)_N = -(V)_1 \tag{8.9.28}$$

where V is the total velocity at the two control points. The off-body total velocities are computed from

$$V = \frac{(V^n)^2 + (V^t)^2}{V} = V^n \frac{V^n}{V} + V^t \frac{V^t}{V} = V^n \sin\phi + V^t \cos\phi \tag{8.9.29}$$

where V^n and V^t are computed by expressions identical to those given by Eqs. (8.9.12) at the two off-body control points, $I = 1$, $I = N$, that is,

$$(V^n)_I = \sum_{j=1}^{N} A_{Ij}^{n} q_j + \tau \sum_{j=1}^{N} B_{Ij}^{n} + V_\infty \sin(\alpha - \theta_I) \tag{8.9.30a}$$

$$(V^t)_I = \sum_{j=1}^{N} A_{Ij}^{t} q_j + \tau \sum_{j=1}^{N} B_{Ij}^{t} + V_\infty \cos(\alpha - \theta_I) \tag{8.9.30b}$$

and where

$$\phi = \tan^{-1}\left[(V^n)_I / (V^t)_I\right] \tag{8.9.31}$$

With Eqs. (8.9.30), the expression for the total velocity given by Eq. (8.9.29) can be written as

$$V = \sum_{j=1}^{N} \left(A_{Ij}^{n} \cdot \sin\phi + A_{Ij}^{t} \cdot \cos\phi\right) q_j + \tau \sum_{j=1}^{N} \left(B_{Ij}^{n} \cdot \sin\phi + B_{Ij}^{t} \cdot \cos\phi \right. \tag{8.9.32a}$$

or as

$$V = \sum_{j=1}^{N} A'_{Ij} q_j + \tau \sum_{j=1}^{N} B'_{Ij} + V_\infty \cos(\alpha - \theta_I - \phi) \tag{8.9.32b}$$

where

$$A'_{Ij} = A_{Ij}^{n} \cdot \sin\phi + A_{Ij}^{t} \cdot \cos\phi, \quad B'_{Ij} = B_{Ij}^{n} \cdot \sin\phi + B_{Ij}^{t} \cdot \cos\phi \tag{8.9.33a}$$

$$A_{Ij}^{n} = \frac{1}{2\pi}\left[\sin(\theta_I - \theta_j) \ln\frac{r_{I,j+1}}{r_{Ij}} + \cos(\theta_I - \theta_j)\beta_{Ij}\right] \tag{8.9.33b}$$

$$A_{Ij}^{t} = \frac{1}{2\pi}\left[\sin(\theta_I - \theta_j)\beta_{Ij} - \cos(\theta_I - \theta_j) \ln\frac{r_{I,j+1}}{r_{Ij}}\right] \tag{8.9.33c}$$

$$B_{Ij}^{n} = -A_{Ij}^{t}, \quad B_{Ij}^{t} = A_{Ij}^{n} \tag{8.9.33d}$$

If we define

$$\theta'_I = \theta_I + \phi \tag{8.9.34}$$

then it can be shown that Eq. (8.9.32b) can be written as

$$V = \sum_{j=1}^{N} A'_{Ij} q_j + \tau \sum_{j=1}^{N} B'_{Ij} + V_\infty \cos(\alpha - \theta'_I) \tag{8.9.35}$$

where

$$A'_{Ij} = \frac{1}{2\pi}\left[\sin(\theta'_I - \theta_j)\beta_{Ij} - \cos(\theta'_I - \theta_j) \ln\frac{r_{I,j+1}}{r_{Ij}}\right] \tag{8.9.36a}$$

$$B'_{Ij} = \frac{1}{2\pi}\left[\sin(\theta'_I - \theta_j) \ln\frac{r_{I,j+1}}{r_{Ij}} + \cos(\theta'_I - \theta_j)\beta_{Ij}\right] \tag{8.9.36b}$$

The off-body Kutta condition can now be expressed in a form similar to that of Eq. (8.9.22). Applying Eq. (8.9.28) to Eq. (8.9.35), we write the resulting expression as

$$\sum_{j=1}^{N} A'_{Nj} q_j + \tau \sum_{j=1}^{N} B'_{Nj} + V_\infty \cos(\alpha - \theta'_N) = -\left[\sum_{j=1}^{N} A'_{1j} q_j + \tau \sum \right. \tag{8.9.37a}$$

or as

$$\sum_{j=1}^{N} (A'_{1j} + A'_{Nj}) q_j + \tau \sum_{j=1}^{N} (B'_{1j} + B'_{Nj}) + V_\infty \cos(\alpha - \theta'_1) + V_\infty \cos \tag{8.9.37b}$$

Read full chapter

URL: https://www.sciencedirect.com/science/article/pii/B9780080983356000082

Surface subsidence characteristics and damage protection techniques of high-intensity mining in China

Guo Wenbing, ... Yang Daming, in Advances in Coal Mine Ground Control, 2017

6.1.1.2 The technical parameters and characteristics of high-intensity mining

The main technical parameters of high-intensity mining are mining method, panel length, and width, face advance velocity, mining height, and annual output. The large mining height fully mechanized coal mining and fully mechanized caving mining method are most widely used in China.

a. **Panel sizes**: The panel width of high-intensity mining is mostly larger than 200 m, with a majority ranging from 200 to 300 m, and the maximum more than 400 m. The face advance mostly ranges from 1000 to 5000 m/yr, with the maximum more than 6000 m.
b. **Face advance velocity**: Statistics show that the face advance velocity of high-intensity mining ranges from 5.0 to 15.57 m/d. Generally, the face advance velocity of fully mechanized caving mining is smaller than that of large mining height fully-mechanized coal mining.
c. Coal seam thickness: The coal seam thickness of high-intensity mining is greater than 3.5 m, and the maximum is 8.0 m when large mining height fully-mechanized coal mining is used. At present, the super-high shield (mining height is 8.8 m) had been developed successfully by Zhengzhou Coal Mining Machinery Group Co., Ltd. In China, Tashan coal mine had done the industrial test successfully, with the average coal seam thickness 18.44 m by the fully mechanized top coal caving mining method (Ming and Baiyun, 2009). In 2014, the large mining height and top coal caving of 14–20 m extra-thick coal seam mining had been successfully implemented.
d. **Annual output**: The fast face advance of high-intensity mining determines the coal production, and the statistics show that the production for a single panel was 5.0–11.30 Mt/yr.

Optical Observation and Discrete Vortex Analysis of Vortex-Flame Interaction in a Plane Premixed Shear Flow

NorioOhiwa , Yojiro Ishino, in Engineering Turbulence Modelling and Experiments 6, 2005

Flow Model and Assumptions Introduced

In this investigation the reactive flow after the spark-ignition in the two-dimensional confined duct is numerically analyzed by combining the panel method and the discrete vortex method [Ishino et al. (1992)]. The two-dimensional flow model is presented in Figure 3(b). The higher and lower uniform mixture streams having an equal equivalence ratio are separated by the splitter plate and issued from the right- and left-hand side sections having an equal width of $H/2$, respectively, and meet at the downstream end of the splitter plate, at which the two-dimensional shear layer starts and the origin of the two-dimensional coordinate system is set, $Z = (X,Y) = (0, 0)$; $Z = X + iY$. To simplify the numerical simulation, the following assumptions are introduced; (1) the objective flow is two-dimensional and incompressible, (2) the flame zone is so thin compared with the turbulence scale as to be considered as a front of discontinuity, (3) the laminar burning velocity is constant, (4) the vortices entering into the burnt gas region become ineffective due to intense viscosity, and (5) the vorticity generation due to the baroclinic effect and the three-dimensionality of vortex-flame interaction are neglected.

Computational Methods for the Investigations of Heat Transfer Phenomena in Aerospace Applications

Bengt Sundén, Juan Fu, in Heat Transfer in Aerospace Applications, 2017

10.1 Introduction

Computational methods started to have a significant impact on the analysis of aerodynamics and its design in the late 1960s. The so-called panel methods were introduced, and these were based on the distribution of surface singularities on a given configuration. Potential flows (nonviscous flows) around bodies could be solved by these methods. Additional capabilities were added later to the surface panel methods and then it was possible to include higher order more accurate formulations, lifting capability, unsteady flows, and coupling with various boundary layer formulations. However, the panel methods could not offer accurate solutions for high-speed nonlinear flows of current interest, and thus more sophisticated models of the flow field equations had to be developed. Gradually, this development has led to what is now called computational fluid dynamics (CFD). For further details, see Ref. [1].

CFD is an interdisciplinary branch of science and engineering with a broad spectrum of applications. Fluid flow, heat transfer, mass transfer, combustion, and chemical reactions appear in most aspects of modern life and are of significance in automotive, space and aviation, and chemical and process industries, as well as in atmospheric science, energy, medicine, microtechnology, and nanotechnology. The development and applications of CFD have been tremendous, and CFD is used both as a modeling tool and in R&D in many industries nowadays. Besides it continues to be developed for new challenges and is being used in basic research at universities.

In aerospace applications, the fluid flow is compressible and the fluid density varies with its pressure. The flow speed is commonly high and the Mach number is greater than 0.3. Subsonic compressible flows have been found to have a Mach number between 0.3 and 0.8. The relationship between pressure and density is weak, and no shocks will be computed within the flow. Highly compressible flows have a Mach number greater than 0.8. The pressure strongly affects the density, and shocks are possible. Compressible flows can be either transonic ($0.8 < Ma < 1.2$) or supersonic ($1.2 < Ma < 3.0$). In supersonic flows, pressure effects are transported only downstream. The upstream flow is not affected by conditions and obstructions downstream.

The total temperature, T_t, is a key parameter and is the sum of the static temperature and the dynamic temperature. There are two ways to calculate the total temperature, see Eq. (10.1):

$$\mathbf{T_t = T + \frac{V_f^2}{2c_p} \quad and \quad T_t = T\left(1 + \frac{\gamma-1}{2}Ma^2\right)} \tag{10.1}$$

where V is the velocity and c_p is the gas specific heat.

The total pressure, P_t, is another useful quantity for running compressible analyses. It is the sum of the static pressure and the dynamic pressure.

In general, compressible flow analyses are much more sensitive to the applied boundary conditions and material properties than incompressible analyses. If the applied settings do not define a physically real flow situation, then the analysis can be very unstable and may fail to reach a converged solution. Proper specification of the boundary conditions and material properties will greatly improve the chances of a successful analysis.

To include heat transfer in a compressible analysis, it is recommended to apply the total (stagnation) temperature boundary conditions instead of static temperatures at the inlets. Total temperature should also be applied to any solids or walls with known temperature conditions. When there is heat transfer in a compressible analysis, viscous dissipation, pressure work, and kinetic energy terms are calculated. It is very important that the total temperature is specified correctly.

In this chapter a brief summary of the CFD methods, including turbulence modeling; associated problems; and limitations is provided. Examples of CFD applications in aerospace engineering are also provided. Commercially available computer codes and in-house codes are briefly described.

Manoeuvring

In The Maritime Engineering Reference Book, 2008

(b) Boundary Element (Surface Panel) Methods

In the early 1960s, as a consequence of increased computing power, a new numerical approach to the lifting surface problem, known as the panel method or boundary element method began to emerge. This method promised to overcome many of the problems of the early lifting line and the later vortex lattice approach. The technique allowed the treatment of more complex geometries, and actually models the lifting surface itself, allowing the effects of thickness and camber to be calculated. The basic principle of the panel method is based on the linear superposition of source/sinks, vortices and/or doublet elements over the lifting surface, such that the boundary conditions are satisfied on the body, across the wake and in the far field. See also Section 8.17.

Extensive research has been carried out in this field. A detailed overview of this method is provided by one of the pioneers of panel methods, Hess (1990).

The advantage of this approach is that it can be used to model actual geometries without requiring further simplification of the geometry. Although panel methods are more complex than lifting-line methods, the computational effort required is still less than that needed for RANS methods. A panel code used to solve a 3-D rudder flow required only 1% of the computational effort needed by a RANS code to solve the same flow problem, Turnock and Wright (2000). The advantage of the panel method is that computations are carried out to determine unknowns only on the body, wake, and far field boundary surfaces, and not throughout whole fluid domain.

Panel methods allow considerable freedom in their numerical application so that complex flow features (rotational and viscous) such as wake roll up, separation zones and unsteadiness can be incorporated. However, as a potential flow method they, like the lifting-line method, cannot account directly for frictional drag, separation and stall effects.